International Journal of Nanomedicine

Dovepress
open access to scientific and medical research

Open Access Full Text Article

ORIGINAL RESEARCH

Biodegradable nanotheranostics with hyperthermia-induced bubble ability for ultrasound imaging–guided chemo-photothermal therapy

This article was published in the following Dove Press journal:
International Journal of Nanomedicine

Changsong Xu[1,2,*]
Feng Gao[3,*]
Jianrong Wu[4]
Shiwei Niu[4]
Fan Li[3]
Lifang Jin[3]
Qiusheng Shi[3]
Lianfang Du[1,3]

[1]Department of Ultrasound, Shanghai General Hospital of Nanjing Medical University, Shanghai 201600, People's Republic of China; [2]Department of Ultrasound, The Affiliated Huaian No.1 People's Hospital of Nanjing Medical University, Huai'an City, Jiangsu 223300, People's Republic of China; [3]Department of Ultrasound, Shanghai General Hospital, Shanghai Jiaotong University School of Medicine, Shanghai 201600, People's Republic of China; [4]College of Chemistry, Chemical Engineering and Biotechnology, Donghua University, Shanghai 201620, People's Republic of China

*These authors contributed equally to this work

Correspondence: Qiusheng Shi
Shanghai General Hospital, Shanghai Jiaotong University School of Medicine, 650 Xin Songjiang Road, Songjiang District, Shanghai 201600, People's Republic of China
Tel +86 1 338 625 9562
Fax +86 0 213 779 8276
Email sqs19631989@163.com

Lianfang Du
Department of Ultrasound, Shanghai General Hospital of Nanjing Medical University, 650 Xin Songjiang Road, Songjiang District, Shanghai 201600, People's Republic of China
Tel +86 1 338 625 9562
Fax +86 0 213 779 8276
Email lianfang_du@126.com

Background: Theranostics, elaborately integrating both therapeutic and diagnostic functions into a nanoplatform holds great potential for precision cancer medicine.

Methods: Herein, a biodegradable theranostic nanoplatform with hyperthermia-induced bubble ability for highly efficient ultrasound (US) imaging–guided chemo-photothermal therapy of breast tumors was developed. The prepared nanoparticles consisted of polydopamine (PDA)-modified hollow mesoporous organosilica nanoparticles (HMONs) with approximately 75 nm in diameter for doxorubicin (DOX) loading and perfluoropentane (PFP) filling. In addition, the pH-sensitive PDA coating served as both gatekeeper controlling DOX release and photothermal agent for inducing hyperthermia.

Results: Such nanoplatform (PDA@HMONs-DOX/PFP, PHDP) provides efficient loading (328 mg/g) and controllable stimuli-responsive release of DOX for chemotherapy. The incorporated disulfide bonds in the framework of HMONs endowed nanoparticles with intrinsic glutathione-responsive biodegradability and improved biocompatibility. Benefiting from the hyperthermia upon an 808-nm laser irradiation of PDA, the liquid–gas phase transition of the loaded PFP was induced, resulting in the generation of the nanobubbles, followed by the coalescence into microbubbles. This conversation could enhance the tumor cell uptake of nanoparticles, as well as intensify the US imaging signals. In addition, a synergistic therapeutic effect of our fabricated nanoplatform on cells/tumor growth effect has been systematically evaluated both in vitro and in vivo.

Conclusion: Therefore, such "all-in-one" PHDP nanoparticles with satisfactory biocompatibility and biodegradability, hyperthermia-induced bubble ability and simultaneous US imaging performance hold great potential for cancer nanotheranostics.

Keywords: biodegradable, bubble, hollow mesoporous organosilica, nanotheranostics, synergistic therapy

Introduction

Cancer incidence and mortality are rapidly growing worldwide.[1,2] Although progress has been realized recently, only limited success was achieved owing to the complexity and heterogeneity of tumor.[3–5] With the development of nanobiotechnology in biomedicine, various nanosystems based on inorganic and organic functions have been designed and their potential applications for cancer management have been investigated.[6,7] More recently, among the numerous kinds of nanosystems, inorganic nanoplatforms have gained considerable momentum due to their unique features, such as multifunctionality, excellent biocompatibility, and ability to

avoid the unpredictable toxicity risks.[8–11] Thus, several stimuli-triggered biodegradable theranostic nanoplatforms based on inorganic nanomaterials have been fabricated.

Among various nanosystems, biodegradable mesoporous silica nanoparticles (MSNs) have become an even more attractive alternative to the traditional organic or inorganic nanomaterials in molecular imaging,[12] biosensing,[13] and drug delivery.[14–16] As an ideal carrier, mesoporous organosilica nanoparticles (MONs) have been widely used for loading various therapeutic/diagnostic modalities because of their well-defined morphology, large surface areas, unique tumor-sensitive biodegradability, and high biocompatibility.[17,18] Congeneric hybridization/incorporation of functional organic groups into the skeleton is a potential strategy to fabricate the MONs, which achieve tumor microenvironment-triggered biodegradation.[17] The direct incorporation of disulfide bonds into the framework has been proved as an effective strategy because it can specifically respond to the intracellular reducing microenvironment within the tumor tissue.[15,19,20] For instance, Huang et al prepared biodegradable mesoporous nanosonosensitizers based on hollow mesoporous organosilica nanoparticles (HMONs) with disulfide bonds containing a framework for the delivery of both DOX and protoporphyrin to realize synergistic sonodynamic and chemotherapy of tumor.[13] Also, Wu et al developed a gemcitabine-gated biodegradable HMONs nanosystem for the controlled delivery of heat shock protein 90 inhibitor and indocyanine green for multidual imaging-guided chemotherapy and low-temperature photothermal therapy.[20] Despite that those inspiring results were achieved, there are still great demands to explore novel MONs-based nanoplatform to extend their application in cancer theranostics.

As a noninvasive technique,ultrasound (US) imaging is commonly used in the clinic with the advantages of low cost, safety, and easy access to the public.[21–23] Currently, highly echogenic microbubbles (MBs) in the state of gas precursor–contained microbubbles have been commonly used in clinical to enhance the US image quality due to their unique noninvasive feature in the dynamic detection of the micro- and macro-vasculature by tissue perfusion.[24] However, MBs are still less stable, nonspecific, and only realize vasculature and blood-flow imaging.[25] To overcome these limitations, nanosized US-enhanced-contrast agents were further explored for extensive biomedical applications, which exhibit analogous contrast effect with contrast agents in microsize, as well as possess enhanced tumor accumulation in vivo.[21,26] Unfortunately, the US responsiveness is deteriorated gradually with the size of MBs decreasing into nanoscale. Also, it has been well proven that micro/nanoparticles can act as the drug-delivery system for enhanced chemotherapy. Therefore, the micro/nanoparticle-based synergistic agents can realize the function for enhancing the chemotherapy.[24] Thus, several strategies have a focus on the phase-transformable strategy with excellent responsiveness for US imaging–guided theranostics. The rational design of bubble-generating nanoplatforms could also realize the controlled payloads releasing for synergistic US imaging and chemotherapy.[26] Optical droplet vaporization (ODV) is an effective strategy to trigger the liquid–gas phase transformation of nanodroplets to form MBs because it could be simply achieved by combining distinctive component to induce heat and phase-shifting droplet.[27,28] For instance, Fokong et al reported poly(n-butyl cyanoacrylate)-based MBs loaded with hydrophilic (rhodamine-b) and hydrophobic (coumarin-6) model drugs and demonstrated efficient US-mediated release of these drugs in vitro and in vivo in tumor-bearing mice.[29] However, the development of a biodegradable nanoplatform with a macrovoid to encapsulate the perfluorocarbons and avoid long-term toxicity is still highly desired.

In this work, an "all-in-one" nanotheranostic agent has been constructed with distinctive biodegradability in the tumor microenvironment and high penetration ability of US imaging as well as remarkable synergetic chemo-photothermal therapy. The organic–inorganic hybridized HMONs with disulfide bond in the framework were prepared. The hydrophobic perfluoropentane liquid (PFP, boiling point of 29°C)[30] and doxorubicin (DOX) were also simultaneously encapsulated into the hollow interior of HMONs. Furthermore, the pH-sensitive PDA coating was introduced to obtain the nanotheranostics (PDA@HMONs-DOX/PFP, PHDP) (Figure 1). The PDA coating prevents the premature release of encapsulated contents and endows the PHDP with the pH-responsive DOX release property for chemotherapy. Subsequently, the PDA could effectively convert the absorbed near infrared (NIR) into hyperthermia upon NIR laser irradiation for photothermal therapy (PTT). Furthermore, the encapsulated liquid PFP was vaporized upon the heat and transformed into microbubbles, thus intensifying the US imaging signal. Prospectively, the developed PDA-anchored biodegradable nanotheranostics with hyperthermia-induced bubble ability could perform the

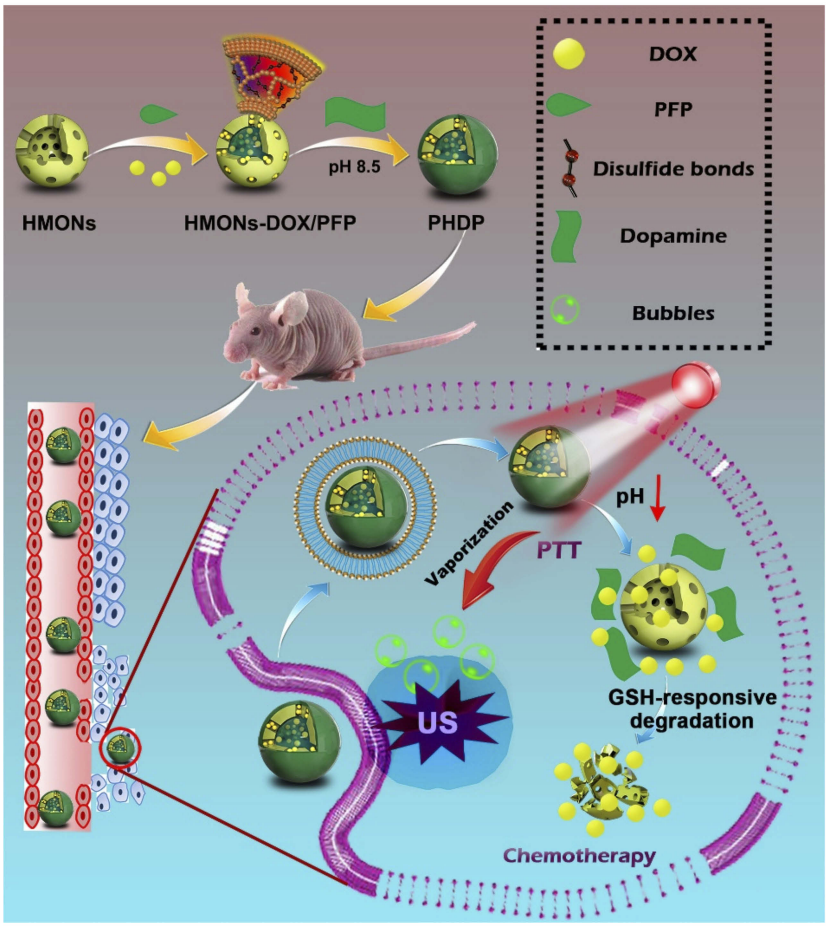

Figure 1 Schematic of the construction of PHDP nanoplatform for US imaging, hyperthermia-induced PFP bubble release, and synergistic chemo-photothermal therapy.
Abbreviations: HMONs, hollow mesoporous organosilica nanoparticles; DOX, doxorubicin; PFP, perfluoropentane; PDA, polydopamine; PHDP, PDA@HMONs-DOX/PFP; PTT, photothermal therapy; GSH, glutathione; US, ultrasound.

enhanced US imaging–guided chemo-PTT of tumor, which holds great potential for cancer nanotheranostics.

Experimental

Materials

Tetrathylorthosilicate, triethanolamine, ammonia solution, dimethyl sulfoxide, and dopamine hydrochloride were supplied from Sinopharm Chemical Reagent Co. Ltd (Shanghai, China). MTT, glutathione (GSH), calcein AM, propidium iodide (PI), DAPI and cetyltrimethyammoniumchloride were obtained from Sigma-Aldrich (St. Louis, MO). Doxorubicin (DOX) was provided from Beijing HuaFeng United Technology Co., Ltd (Beijing, China). 3-Aminopropyltriethoxysilane and bis[3-(triethoxysilyl)propyl]tetrasulfide were obtained from Aladdin Reagent Co. Ltd. (Shanghai, China). Perfluoropentane (PFP) was purchased from Energy Chemical Co., Ltd. (Shanghai, China). FBS, DMEM, penicillin-streptomycin solution 0.05% trypsin-EDTA and PBS were purchased from Gibco (Invitrogen, Carlsbad, CA). Human breast cancer cell line (MDA-MB-231cells) and A549 cells were supplied by the Institute of Biochemistry and Cell Biology (Chinese Academy of Sciences, Shanghai, China). A Milli-Q plus 185 water purification system (Millipore, Bedford, MA) was used to treat water to have a resistivity higher than 18.2 MΩ.cm. All chemicals were used without other treatments.

Synthesis of PHDP nanoparticles

First, HMONs were synthesized according to a reported method.[13] Then, 25 g of HMONs was placed in a 50-mL centrifuge tube. After vacuuming, 200 μL of PFP was rapidly injected into the tube, followed by US sonication in an ice bath for 2 mins and PFP-loaded HMONs (PFP@HMONs) were obtained and then dispersed in 20 mL of PBS for further use. Subsequently, DOX hydrochloride (50 mg) dissolved in 10 mL PBS was added into

10 mL of PFP@HMONs suspension and stirred at room temperature in the dark. After 24 hrs, the products (designated as HMONs-DOX/PFP) were collected by centrifugation and washed with PBS for several times to remove the unloaded DOX. Meanwhile, the DOX loading capacity was determined by measuring the absorbance of HMONs-DOX/PFP at 480 nm and calculated by the following equations

$$LC = (\text{weight of loaded DOX})/(\text{total weight of DOX loaded PFP@HMONs}) \times 100\% \quad (1)$$

After that, 50 mg of HMONs-DOX/PFP was suspended in 50 mL of Tris buffer solution (pH =8.5, 10 mM) containing dopamine hydrochloride (0.65 mg/mL). Then, the solution was stirred at room temperature for 6 hrs to allow for the self-polymerization of dopamine. After that, the black products were collected by centrifugation and washed with water for several times. The final product (PDA@HMONs-DOX/PFP, designated as PHDP) was re-suspended in PBS for further use.

Characterization

Transmission electron microscopy (TEM) was employed to observe the morphology of samples at an operating voltage of 200 kV (TEM, JEOL 2010F, Tokyo, Japan). N_2 adsorption/desorption isotherms were measured by an ASAP 2020 absorption analyzer (Micromeritics, Atlanta, GA, USA). Brunauer–Emmett–Teller (BET) and Barrett–Joyner–Halenda methods were used to determine the specific surface area and pore size, respectively. Solid-state ^{13}C CP/MAS and ^{29}Si NMR spectra of nanoparticles were captured from the 500-MHz solid NMR spectrometer (AVANCE III HD, Bruker, Switzerland). Fourier transform infrared spectra were analyzed by IRPrestige-21 spectrometer (Shimadzu, Japan). Thermogravimetric analysis (TGA) of nanoparticles was carried out by a thermal gravimetric analyzer (Netzsch STA 449, Germany). Zeta potential and hydrodynamic particle size were determined on Malvern Zetasizer Nanoseries (Nano ZS90). UV-Vis-NIR spectra of samples were obtained on a Lambda 35 spectrophotometer (PerkinElmer, USA). The Si concentration was determined by an inductively coupled plasma-optical emission spectroscopy (ICP-OES, Leeman Prodigy, Hudson, NH).

Photothermal properties of PHDP nanoparticles

To evaluate the photothermal conversion performance of the PHDP nanoparticles, 0.2 mL of PHDP dispersions at different concentrations (0–200 μg/mL) was exposed to an NIR laser (808 nm, Beijing STONE Laser, China) at a power density of 1.0 W cm^{-2} for 5 mins. Next, 0.5 mL of PHDP dispersions (200 μg/mL) was irradiated at different power intensities (0.4–1.2 W/cm^2) for 5 mins. The temperature change of the samples was recorded by a thermocouple (Shenzhen Everbest Machinery Industry Co., Ltd., Shenzhen, China). Finally, the photothermal conversion efficiency (η) of the PHDP nanoparticles was calculated by the following equation that reported in the previous literature.[14,18]

$$\eta = \frac{hS(T_{max} - T_{am}) - Q_0}{I\left(1 - 10^{-A}\right)} \quad (2)$$

where h is heat transfer coefficient, S stands for the surface area, T_{max} is equilibrium temperature, T_{am} is surrounding ambient temperature, Q_0 is heat absorption of quartz cell, I express the laser power, and A is the absorbance of PHDP at 808 nm.

In vitro DOX release

To determine the pH- and GSH-triggered DOX release, 2 mL of PHDP dispersion (1.25 mg/mL) was added in a dialysis bag (cutoff MW: 5000 Da) and then put in PBS (pH 5.0 or 7.4) solution with or without the addition of 10 mM GSH, which was then put in a shaker at 37ºC with the speed of 100 rpm. After that, the release buffer was taken out at designated time intervals and the amount of released DOX was determined by UV-Vis analysis.

In vitro bubble release and US imaging of PHDP

For the measurement of bubble release, 0.5 mL PHDP containing PBS solution (5 mg/mL, with or without 10 mM of GSH) was placed onto a glass slide and covered with a coverslip. After that, the PHDP samples were exposed to an 808-nm NIR laser at the power intensity of 0.8 W/cm^2. At each time point, the bubble production was observed by an Olympus IX81 microscopy (Tokyo, Japan). To investigate the US imaging ability of the produced PFP bubbles, PHDP nanoparticles were dispersed in PBS (20 mg/mL). Both US images and videos before and after 808-nm NIR irradiation (0.8 W/cm^2, 5 mins) were simultaneously recorded on an IU-Elite US imaging system (Philips, Eindhoven, Netherland). The corresponding gray values were calculated by using Image J software.

In vitro cytotoxicity and cellular uptake assays

MDA-MB-231 and A549 cells were cultured in DMEM supplemented with 10% (v/v) FBS. All cells were maintained in a 5% CO_2 atmosphere at 37°C. To study the cytotoxicity of PDA@HMONs-PFP nanoparticles, MDA-MB-231 and A549 cells (1×10^4) were seeded into 96-well plate and incubated overnight. Then, the old culture medium in each well was removed and replaced with different concentrations of PDA@HMONs-PFP (50, 100, 150, 200, and 250 μg mL^{-1}). After incubation for another 24 hrs, the cells in each well were washed with PBS and the cell viabilities were determined by a standard MTT assay.

The cellular uptake of PHDP nanoparticles was performed by using flow cytometry and ICP-OES. For flow cytometry, MDA-MB-231 cells were seeded into 6-well plate at a density of 2×10^5 cells per well and then incubated overnight. Then, the cell medium in each well was replaced with 100 μL of DMEM containing free DOX or PHDP at an equivalent DOX concentration (10 μg mL^{-1}) and incubated for another 4 hrs. After that, the cells were trypsinized, harvested by centrifugation and suspended in PBS. Meanwhile, the intracellular fluorescence of DOX was determined by a flow cytometer (BD Biosciences, San Jose, CA, USA) at an excitation wavelength of 488 nm. For ICP-OES analysis, 200 μL of DMEM containing PHDP was incubated with MDA-MB-231 cells in 12-well plates at a density of 2×10^5 cells per well, and the cells were incubated for 2, 4, or 8 hrs, respectively. Thereafter, the cells were washed twice with cold PBS, trypsinized, harvested and suspended in 1 mL of PBS for counting the cell numbers. Subsequently, the cells were digested by aqua regia solution (1.0 mL) overnight, followed by ICP-OES assay to measure the Si concentration in every sample.

In vitro synergistic chemo-PTT therapy

MDA-MB-231 cells (2×10^4 cells/well) were seeded in 96-well plates and then incubated for 24 hrs. Then, the cell culture medium was removed and replenished with fresh DMEM containing different concentrations of free DOX, PDA@HMONs-PFP, and PHDP. The free PDA group was used as a reference. After incubation for another 12 hrs, half of the cells treated with PDA@HMONs-PFP and PHDP were exposed to an 808-nm laser (0.8 W cm^{-2}) for 5 mins. After the total incubation time of 24 hrs at 37°C, the cell viability after different treatments was analyzed by the standard MTT assay. Also, the cells after different treatments were stained with calcein-AM and PI solutions at the same concentration of 4×10^{-6} M. After a culture for another 20 mins, the cells were washed with PBS and monitored with an Axio Vert A1 inverted fluorescence microscope (Carl Zeiss, Jena, Germany).

In vivo US imaging

Female BAlB/c nude mice (5-week-old, 15–20 g) were supplied by Shanghai Slac Laboratory Animal Center (Shanghai, China). All the animal experiments were performed following the guidelines of the ethical committee of Shanghai Jiaotong University Animal Care and Use Committee and also the policy of the National Ministry of Health. Animal protocols were approved by the Shanghai Jiaotong University Animal Care and Use Committee. To develop the MDA-MB-231 tumor model, mice were subcutaneously injected with 2×10^6 MDA-MB-231 cancer cells (suspended in 50 μL PBS) on the right hind leg of each mouse. The tumor size of each mouse after different treatments was measured every 2 days with a caliper and the volume (V) was calculated as $V = 1/2\times L\times W^2$ (L, W is long diameter and short diameter, respectively). When the tumor reached a volume of about 0.1 cm^3, the mice were anesthetized and i.v. injected with 100 μL of PBS, PDA@HMONs-DOX and PHDP (10 mg/mL). The US images of the tumor sites were immediately captured at 24 hrs postinjection using a VisualSonics Vevo LAZR system (VisualSonics Inc. NY, USA) before and after NIR laser irradiation (808 nm, 0.8 W cm^{-2}, 10 mins). Also, the mice only treated with NIR laser irradiation were set as a control group. The gray value of the obtained US images was calculated using Image J software.

In vivo chemo-photothermal combined cancer therapy

When the tumor volume reached about 100 mm^3, the mice were randomly divided into 5 treatment groups (n=5). Different treatments were performed as follows: (1) saline, (2) free DOX (5 mg DOX kg^{-1}), (3) PHDP (5 mg DOX kg^{-1}), (4) PDA@HMONs-PFP and treated with NIR irradiation, and (5) PHDP (5 mg DOX kg^{-1}) with NIR irradiation. The tumors in groups 4 and 5 were subjected to NIR laser for 10 mins at 12 hrs postinjection. During which time the tumor temperature was captured by an IRS E50 Pro Thermal

Imaging Camera. The tumor size of each mouse after different treatments was measured every 2 days and the body weight was recorded, and the mice of all treatment groups were sacrificed after the treatment, and the tumors and the main organs, including livers, hearts, lungs, spleens, and kidneys, were harvested to make paraffin section for histological analysis, including H&E and terminal deoxynucleotidyl transferase dUTP nick end labeling (TUNEL) staining and observed under an Olympus IX70 inverted fluorescence microscope. Also, the in vivo biodistribution of PHDP in the tumor-bearing mice was evaluated by ICP-OES according to the previous study.[19]

Statistical analysis

The experimental data were evaluated by one-way ANOVA statistical method. All data were presented as mean ± standard deviation. A value of 0.05 was used as the significance level and the data were indicated with (*) for $P<0.05$, (**) for $P<0.01$, and (***) for $P<0.001$, respectively.

Results and discussion

Preparation and characterization of the PHDP nanoparticles

It has been proved that the disulfide bond can be cleaved in the reductive environment.[17,18] We predicted that the hybridization of disulfide bond into silica framework can endow the HMONs with unique tumor-sensitive biodegradability. Based on "chemical homology" mechanism, organic–inorganic hybridized HMONs nanoparticles with excellent biocompatibility and high dispersity were synthesized.[13,15] It can be observed that the monodispersed MSNs@MONs show a clear core/shell structure with a diameter of around 65 nm (Figure 2A). It is noted that triethanolamine is necessary to acquire the relatively small size of MSNs@MONs.[28] After the MSNs core was etched in ammonia solution, the HMONs with hollow nanostructure were obtained with the size of approximately 75 nm (Figure 2B). Energy-dispersive spectrometry analysis shows the existence and distribution of C, S, Si, and O elements (Figure S1). The representative

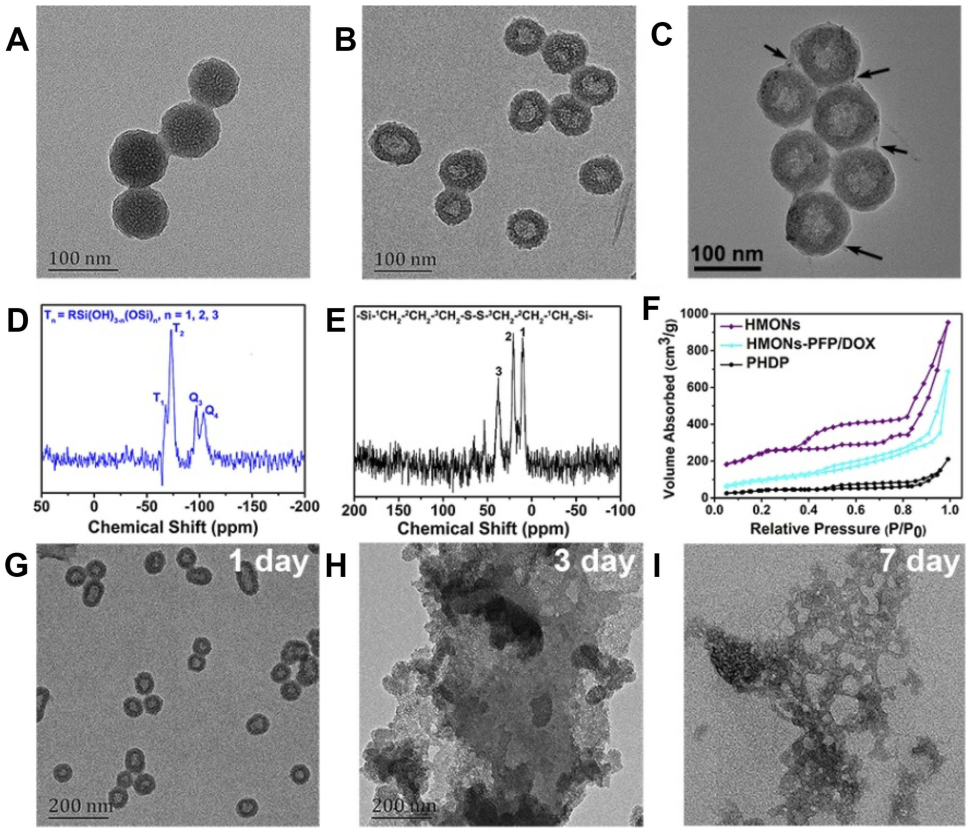

Figure 2 Synthesis and characterization of HMONs nanoparticles.

Notes: TEM images of (**A**) MSNs@MONs, (**B**) HMONs, and (**C**) PHDP nanoparticles. The black arrows indicate the PDA coating. (**D**) ^{29}Si and (**E**) ^{13}C NMR spectra of as-synthesized HMONs. (**F**) N_2 adsorption–desorption isotherms of HMONs, HMON-PFP/DOX, and PHDP. TEM images of HMONs dispersed in PBS containing GSH (10 mM) for (**G**) 1 day, (**H**) 3 days, and (**I**) 7 days.

Abbreviations: TEM, transmission electron microscopy; MSNs@MONs, solid silica core/mesoporous silica shell nanospheres; HMONs, hollow mesoporous organosilica nanoparticles; PHDP, PDA@HMONs-DOX/PFP; DOX, doxorubicin; PFP, perfluoropentane; NMR, nuclear magnetic resonance; GSH, glutathione.

Q and T silicon sites were observed from the ^{29}Si MAS NMR spectrum of HMONs (Figure 2D), indicating the coexistence of the hybrid silsesquioxane within the framework of HMONs.[20] Also, the peaks of ^{13}C NMR spectrum at 42.2, 23.5, and 12.3 ppm corresponded to the sites of ^{3}C, ^{2}C, and ^{1}C in the series of -Si-$^{1}CH_2$-$^{2}CH_2$-$^{3}CH_2$-S-S-S-S-$^{3}CH_2$-$^{2}CH_2$-$^{1}CH_2$-Si-, respectively (Figure 2E).[19] Meanwhile, the N_2 absorption–desorption isotherm of HMONs exhibited the presence of mesoporous structure and the surface area and pore size was calculated to be of 835.1 m^2/g and 3.64 nm, respectively (Figures 2F and S2), which makes HMONs promising for various payloads (DOX and PFP in this work) delivery.[31] Next, the biodegradation behavior of the prepared HMONs was studied and monitored by TEM observation. Clearly, HMONs were degraded gradually in PBS solution containing GSH with the prolongation of incubation time (Figure 2G–I). It initiated structure collapse, and nanoparticle dissolution after 1 week of biodegradation, almost no regular spherical HMONs can be identified. Thanks to the high concentration of GSH in cancer cells,[18] such HMONs with intrinsic tumor microenvironment-responsive biodegradability are suitable for biological applications.

Owing to the unique hollow cavity, the PFP molecules were loaded into the inner cavity by the mild infusion method.[32] It can be seen that the apparent phase-separated phenomenon occurred between the free PFP and PBS because PFP is hydrophobic, while the PFP-loaded HMONs (HMONs-PFP) can be well dispersed in PBS (Figure S3). Next, DOX was loaded into PFP@HMONs to form the HMONs-PFP/DOX. After the loading DOX into the hollow cavity, the surface potential of HMONs-PFP/DOX increased to −9.3±2.1 mV (Table S1), confirming that the partial negative charge of the silanol groups in the surface of HMON nanoparticles was neutralized by the positively charged amino groups on DOX.[33] UV-vis-NIR spectra of HMONs-PFP/DOX show the characteristic absorption peak of DOX at 480 nm, illuminating the successful loading of DOX onto HMONs-PFP (Figure 3A). The drug loading capacity was further

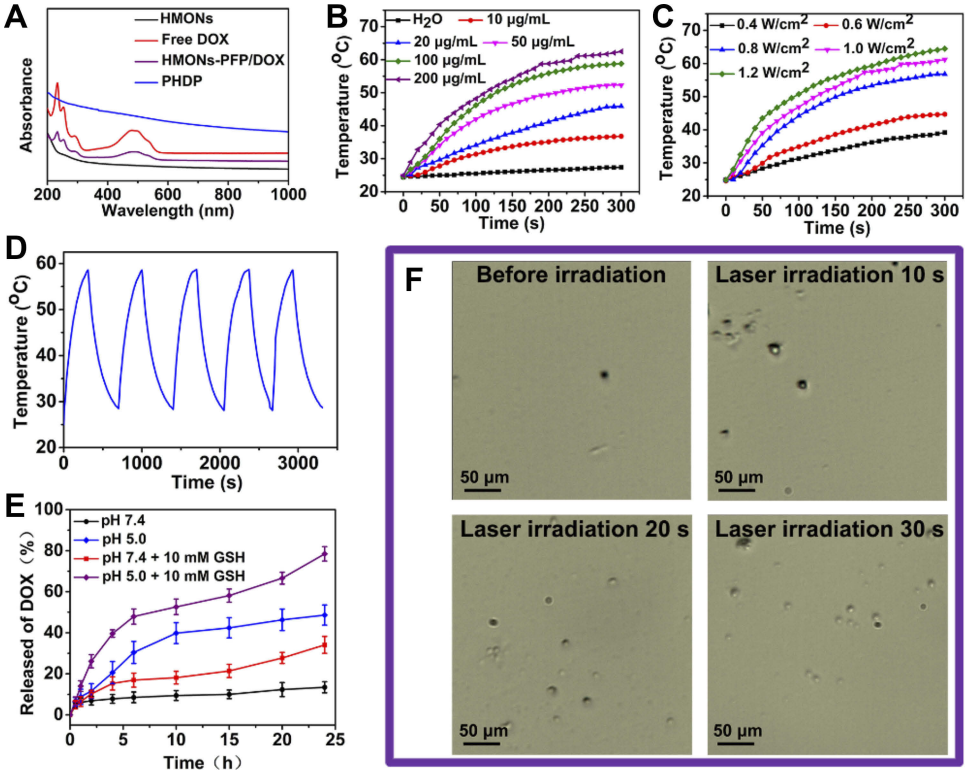

Figure 3 Photothermal properties of PHDP nanoparticles, in vitro drug release and generation of microbubbles.

Notes: (**A**) UV-vis-NIR spectra of HMONs, DOX, HMONs-PFP/DOX, and PHDP nanoparticles. (**B**) Temperature elevation of water and PHDP dispersions with different concentrations under NIR laser irradiation (808 nm, 0.8 W cm^{-2}). (**C**) Temperature of the solution containing PHDP (100 μg/mL) at different laser power density. (**D**) Photothermal stability of PHDP (100 μg mL^{-1}) within five cycles of NIR laser irradiation (0.8 W cm^{-2}). (**E**) Release profiles of DOX at different pHs with or without addition of GSH (10 mM). (**F**) Optical microscopy images of PHDP aqueous solution before and after NIR laser irradiation for 10 s, 20 s, and 30 s.

Abbreviations: HMONs, hollow mesoporous organosilica nanoparticles; PHDP, PDA@HMONs-DOX/PFP; DOX, doxorubicin; PFP, perfluoropentane; NIR, near infrared; GSH, glutathione.

measured. About 328 mg of DOX could be loaded into 1 g of HMONs-PFP nanoparticles. After coating of a PDA shell onto the surface of HMONs-PFP/DOX nanoparticles, the PHDP nanotheranostics were obtained. Obviously, a clear layer on the periphery of the PHDP nanoparticles was observed, which is quite different from that of the HMONs (Figure 2C). Furthermore, TGA analysis was performed and the curves are shown in Figure S4. The weight loss of the bare HMONs nanoparticles was 20.1 wt %. In contrast, the weight loss increased to 35.2 wt % for PHDP, indicating that about 15.1 wt % of PDA was coated onto the surface of the HMONs. The UV-vis-NIR spectrum of PHDP nanoparticles shows a strong NIR absorption feature in the scope of 600–1000 nm (Figure 3A). Meanwhile, the hydrodynamic size of the PHDP was determined to be 125.1 nm and the zeta potential was −17.3 mV (Table S1), which is ascribed to surface pore-decorating of PDA coating. The surface areas of HMONs-PFP/DOX and PHDP calculated by BET method are 362.1 and 179.3 $cm^2 g^{-1}$, and the corresponding mesopore sizes are 2.5 and 1.2 nm, respectively (Figures 2F and S2). These results further confirmed the successful loading of DOX and successful modification of PDA. Then, the stability of PHDP nanoparticles in water, PBS, or DMEM medium was investigated by measuring the hydrodynamic size of the particles via DLS after they were exposed to different aqueous media for 1 week. Clearly, there are no prominent changes of the hydrodynamic size of the particles in a given time period (Figure S5), suggesting that the obtained nanoparticles possess good colloidal stability.

Photothermal property of the PHDP nanoparticles

Next, the photothermal performance of PHDP nanoparticles was evaluated. As expected, the PHDP showed an excellent strong photothermal effect and both concentration-dependent and power density–dependent temperature increases were displayed (Figure 3B and C), in which the highest temperature raised was to 64.5°C at the concentration of 200 μg/mL after being irradiated by 808-nm NIR laser (1.2 W cm^{-2}) for 5 mins. By contrast, the temperature of the water does not change significantly. Meanwhile, an negligible change of the photothermal conversation performance was observed during the five cycles of laser irradiation (Figure 3D), clearly indicating the excellent photostability of PHDP nanoparticles. Lastly, the photothermal conversion efficiency of PHDP was calculated to be 46.7%. The high photothermal conversion efficiency suggests that PHDP nanoparticles can be developed as an effective photothermal agent used for PTT of cancer.

In vitro drug release kinetics

The property of pH and GSH controllable drug release of DOX from the PHDP was further investigated. The HMONs-PFP/DOX showed an obvious burst release with more than 60% DOX release at pH 7.4 within 12 hrs and even over 83% at pH 5.0 (Figure S6). In contrast, less than 15% of DOX is released from the PHDP at pH 7.4 after 24 hrs (Figure 3E), demonstrating that the PDA coating plays a vital role in the prevention of the premature release of DOX. In comparison, the amount of released DOX up to about 48.6% within 24 hrs at pH 5.0, which can be attributed to the cleavage of the PDA coating. Also, the released percentage of DOX was sharply increased to ≈34.1% and ≈78.4% at pH 7.4 and 5.0 over a span of 24 hrs with the addition of GSH. The GSH-triggered DOX release enhancement from PHDP nanoparticles is mainly ascribed to the hydrolyzation of disulfide bond within the framework under the reducing condition. Considering the low pH values and high GSH concentration in cancer cells,[23] the ability of pH/GSH-responsive release of DOX is conducive to the application of PHDP for cancer therapy.

In vitro US imaging of PHDP

Encouraged by the photothermal conversion property of PHDP, the liquid–gas phase transition of the loaded PFP via the hyperthermia induced was evaluated. Note that the temperature was increased to 48°C to induce the generation of microbubbles by adjusting the laser power density at 0.8 W/cm^2 because the boiling point of PFP will rise from the basic 29°C to 45°C in the blood circulation.[29] As shown in Figure 3F, no microbubbles were observed in the presence of laser irradiation, while many more bubbles were produced for PHDP upon NIR irradiation. This confirmed the "small-to-large" transition of PFP induced by NIR laser irradiation. Then, the US imaging capacity of PHDP was further carefully investigated in vitro. As displayed in Figure 4A, weak US signals and no apparent changes were observed for PBS and PDA@HMONs-DOX in both B-mode and contrast-intensified US images. In comparison, the brightness of B-mode images and the gray value (Figure 4B and C) of the PHDP gradually increase before and after laser exposure in B-mode and contrast mode because of liquid–gas phase transformation of PFP by PDA, confirming the potential to use the PHDP nanoparticles for US imaging.

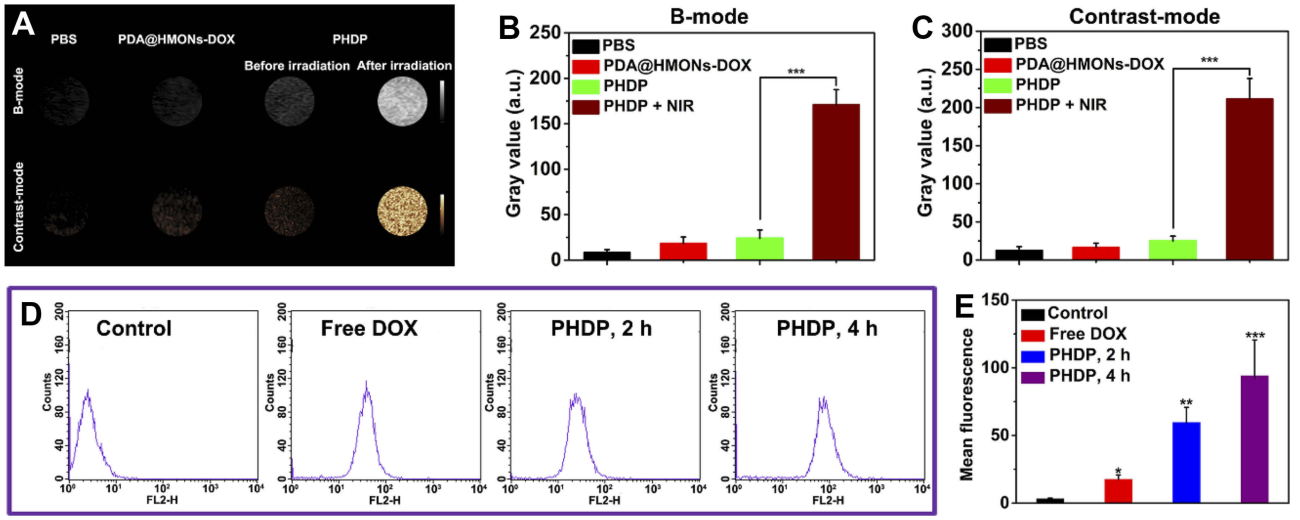

Figure 4 In vitro ultrasound imaging and cellular uptake of PHDP nanoparticles.

Notes: (**A**) US images in B-mode and contrast mode of PBS, PDA@HMONs-DOX, and PHDP nanoparticles before and after NIR irradiation (0.8 W/cm^2, 5 min). (**B, C**) Quantitative analysis of the average gray value in (**A**). (**D**) The flow cytometry data of MDA-MB-231 cells treated with free DOX and PHDP for 2and 4 hrs. (**E**) Quantitative mean fluorescence intensities of the corresponding treated MDA-MB-231 cells. **P*<0.05, ***P*<0.01, ****P*<0.001.

Abbreviations: US, ultrasound; HMONs, hollow mesoporous organosilica nanoparticles; DOX, doxorubicin; PFP, perfluoropentane; PDA, polydopamine; PHDP, PDA@HMONs-DOX/PFP.

In vitro cellular uptake

The cellular uptake was investigated by treating the cells with free DOX or PHDP nanoparticles. The level of the internalization of PHDP nanoparticles into MDA-MB-231 cells was evaluated qualitatively by using flow cytometry and ICP-OES. As shown in Figure 4D, the fluorescence intensities of DOX in cells treated with PHDP after incubation for 2 hrs were much stronger than that of the cells treated with free DOX. Furthermore, the cellular uptake of PHDP nanoparticles could be further increased after incubation for 4 hrs (Figure 4E). These results were also confirmed by ICP-OES analysis. The uptake of Si for the cells incubated with PHDP for 8 hrs was nearly 10 times as high that of incubation for 2 hrs and 3.4-fold of that after 4 hrs of incubation (Figure S7). These results together clearly verified that the PHDP nanoparticles could effectively uptake cancer cells.

In vitro synergistic therapy of PHDP

Next, we evaluated the in vitro synergistic therapy of PHDP with NIR laser irradiation for cancer cells. First, the cytotoxicity of PDA@HMONs-PFP was examined in MDA-MB-231 and A549 cells. No significant cytotoxicity was observed in these two types of cells, even at a high incubation concentration (Figure S8), which indicated the good biocompatibility of PDA@HMONs-PFP. Then, the synergistic effects of photothermal therapy with chemotherapy were further investigated. As shown in Figure 5A, cells incubated with free DOX and PHDP without NIR laser irradiation display a DOX dose-dependent cytotoxic effect. Also, a concentration-dependent toxicity was detected in the PDA@HMONs-PFP and PHDP group after being treated with NIR irradiation (Figure 5B). Particularly, over 95% of the cells died in the synergistic therapy group when treated with PHDP nanoparticles at a concentration of 100 μg mL^{-1} under laser irradiation. For the free PDA group, all the cell viabilities are over 90%, which implies that the PDA coating does not produce cell killing effect. Similar results can be obtained from the fluorescence images of the cells co-stained by calcein AM and PI after different treatments (Figure 5C). For PHDP plus laser irradiation group, most of the cells were dead, while almost all cells remained alive in PBS and laser groups. These results together certified the high therapeutic efficacy of combined chemo-PTT therapy strategy based on the fabricated PHDP nanoplatform.

In vivo US imaging

Encouraged by in vitro US imaging performance of PHDP, in vivo imaging was conducted on MDA-MB-231 tumor--bearing mice after *i.v.* injection with PHDP nanoparticles. There was a faint signal in the tumor site before NIR laser irradiation at 24 hrs postinjection of PHDP (Figure 6A),

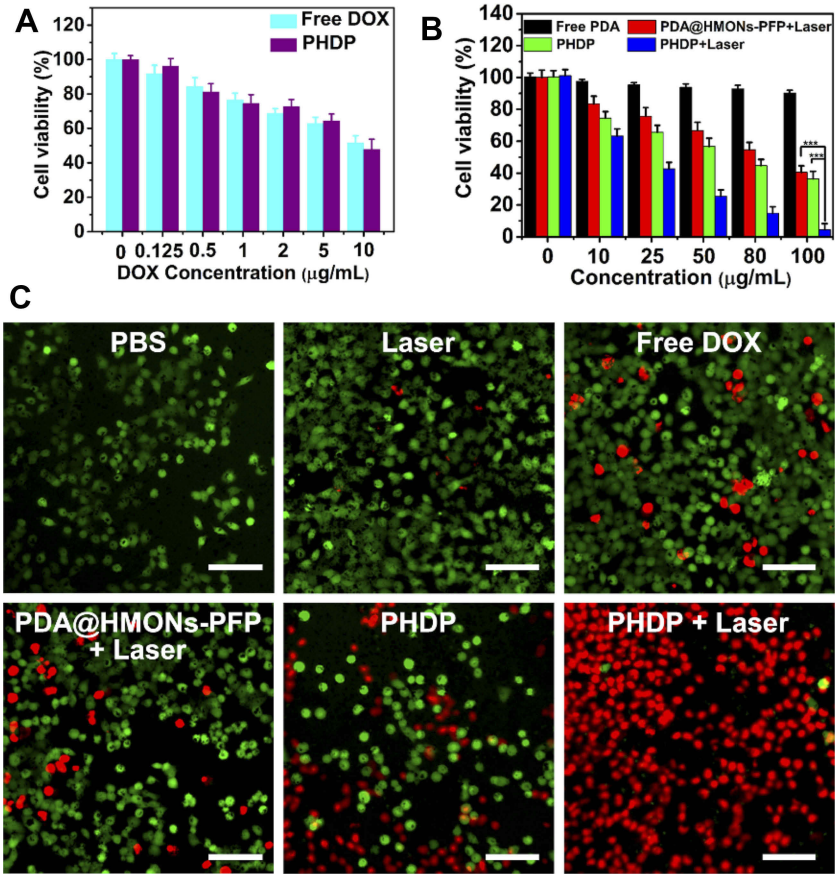

Figure 5 In vitro synergistic therapy.

Notes: (**A**) Relative viabilities of MDA-MB-231 cells after incubation with free DOX and PHDP at various DOX concentrations. (**B**) Relative viability of MDA-MB-231 cells in the presence of various formulations with or without laser irradiation (0.8 W cm^{-2}, 5 mins) and (**C**) corresponding calcein-AM/PI staining images after different treatments (scale bars: 100 μm). ***P<0.01.

Abbreviations: HMONs, hollow mesoporous organosilica nanoparticles; DOX, doxorubicin; PFP, perfluoropentane; PDA, polydopamine; PHDP, PDA@HMONs-DOX/PFP; PI, propidium iodide.

and also no US signal in the tumor at 24 hrs postinjection of PBS or NIR laser irradiation group was observed. These results are attributed to the fact that the liquid–gas change temperature of PFP in the body is higher than the physiological temperature (37 °C) due to the blood/intratumor pressure.[34] After laser irradiation (0.8 W cm^{-2}) for 5 mins, the US signal in both B-mode and contrast mode was significantly enhanced. The reason for this could be because the regional temperature was about 50°C in the tumor, leading to the continuous coalescence into microbubbles. Meanwhile, the average gray value of the tumor region shows that the value after laser irradiation is much higher than that before laser irradiation in both B-mode and contrast mode (Figure 6B). This result confirmed that the developed PHDP enabled valid US imaging and could accumulate to a greater degree in the tumor site.

In vivo chemo-photothermal therapy

Encouraged by these above approving results, the feasibility of employing the PHDP as an ideal nanosystem was further carried out in vivo. First, in vivo distribution of PHDP nanoparticles at specific time points after *i.v.* injection was investigated by using ICP-OES (Figure 6C). The tumor accumulation of Si in mice exhibits a time-dependent pattern and PHDP nanoparticles could efficiently accumulate into tumor tissues with uptake efficiency of 12.3% ID/g at 8 h *i.v.* injection, thus indicating the high accumulation of PHDP nanoparticles. The high tumor accumulation could be universal due to the enhanced permeability and retention effect.[35] Also, PHDP nanoparticles have accumulated in the liver and kidney to some extent, which may be due to the nonspecific uptake by reticuloendothelial cells.[25] The high accumulation of nanoparticles

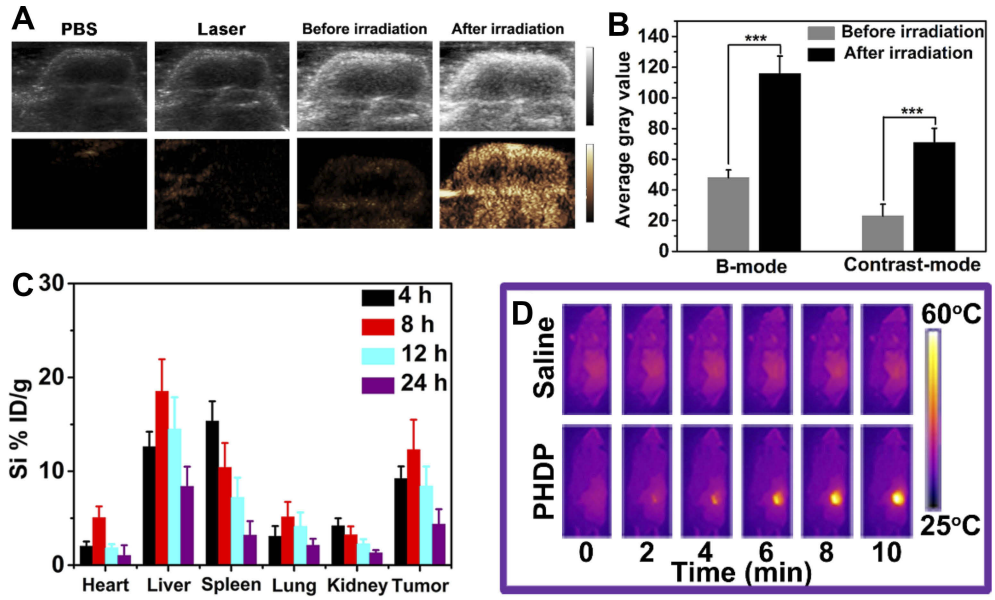

Figure 6 In vivo ultrasound imaging, biodistribution and infrared thermal imaging.
Notes: (**A**) In vivo US images and (**B**) the corresponding gray values of the tumor obtained before and after injected with PHDP nanoparticles before and after NIR laser irradiation 24 hrs postinjection. ***$P<0.001$. (**C**) Time-dependent distribution of PHDP in tumor and various major tissues. The data were shown as mean ± SD (n=3). (**D**) In vivo infrared thermographic maps of mice at 24 h after treatment with control (saline +808 nm) and PHDP +808-nm laser irradiation.
Abbreviations: US, ultrasound; PHDP, PDA@HMONs-DOX/PFP.

confirms that it is expected to be delivered systematically in cancer treatment.

Further, in vivo antitumor study of PHDP nanoparticles on MDA-MB-231 tumor-bearing mice model was further carried out to validate the potential of HDP nanoparticles for in vivo combinatorial cancer therapy. As shown in Figures 6D and S9, the temperature of tumor site in the saline group only increased by <3°C, while the temperature of tumor region in the PHDP group was increased by ≈28ºC to over 60ºC after 10 mins of laser irradiation, which confirmed that the PHDP nanoparticles could act as an ideal photothermal agent for in vivo PTT. As shown in Figure 7A, the mice in the saline group display more than 11-fold increase of tumor volume. Meanwhile, the mice treated with free DOX exhibited minimal tumor inhibition effect because of the limited tumor accumulation. The groups of PHDP and PDA@HMONs-PFP + NIR inhibit the tumor growth to some extent due to the monotherapy effectiveness. Comparatively, after laser irradiation, PHDP nanoparticles can effectively inhibit tumor growth, demonstrating a remarkable synergistic therapeutic effect. This can be also verified from the tumor weight after different treatments (Figure 7B) and photographs of the isolated tumor tissues (inset of Figure 7B). Simultaneously, no significant body weight changes were observed in different treatments (Figure 7C), confirming good tolerance of our fabricated nanoparticles in mice.

Ulteriorly, tumor sections from the sacrificed mice after various treatments were stained with H&E and TUNEL to further clarify the antitumor efficacy. For H&E staining results (Figure 7D), significant large-area apoptosis/necrosis regions in the tumors of PHDP + NIR group, while cancer cells in other groups displayed no notably affected or only partially destroyed. Analogously, maximum apoptosis was observed from the TUNEL-stained images in PHDP + NIR group, which was obviously higher than that of other groups. These are consistent with the above in vivo anticancer treatment results, thus indicating the preeminent inhibition effect of synergistic chemotherapy and PTT by this nanosystem.

Moreover, in vivo biosafety of the PHDP nanoplatform was assessed. According to H&E-stained images of the collected major organs from each group, no evident toxic side effects was observed during the 14-d therapeutic process (Figure S10), demonstrating the good biosecurity of our fabricated nanoplatform. It should be noted that systematic studies are still needed to understand the metabolism and long-term toxicity of nanoparticles. Thus, our elementary toxicity study warrants further exploration of this nanoplatform.

Conclusion

In summary, we have successfully developed an intelligent nanoplatform for US imaging–guided synergistic chemo-

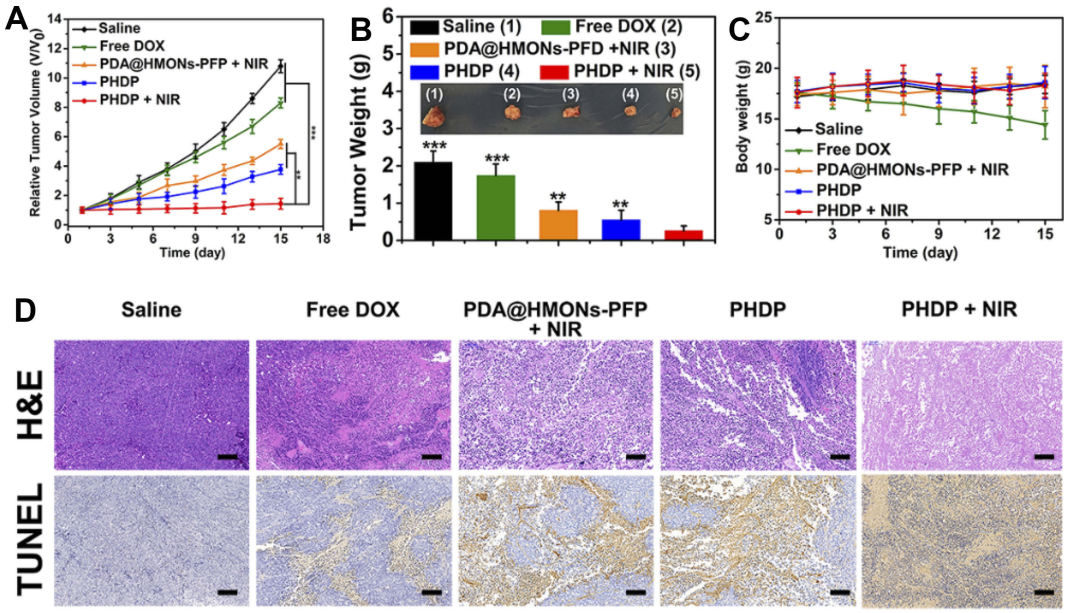

Figure 7 In vivo antitumor activity (n=5).

Notes: (**A**) Time-dependent tumor growth curves (n=5) after different treatments. ***P*<0.01, ****P*<0.001. (**B**) The photographs and the mean tumor weights of the excised tumors after various treatments. ***P*<0.01, ****P*<0.001. (**C**) Time-dependent body weight curves of nude mice (n=5, mean ± s.d.) after different treatments. (**D**) H&E and TUNEL staining of tumor slides from MDA-MB-231 tumor-bearing mice after various treatments. All of scale bars are 100 μm.

Abbreviations: HMONs, hollow mesoporous organosilica nanoparticles; DOX, doxorubicin; PFP, perfluoropentane; PDA, polydopamine; PHDP, PDA@HMONs-DOX/PFP; TUNEL, terminal deoxynucleotidyl transferase dUTP nick end labeling.

photothermal therapy of tumors. This strategy finesses the HMONs-based nanoplatform for the production of nanotheranostics with versatile performance, which has been realized by integrating a hydrophobic PFP and DOX into biodegradable HMONs. Through modification with PDA coating, the as-prepared nanoparticles could reasonably prevent the premature release of the encapsulated contents and showed pH/GSH-responsive DOX release. Importantly, the PDA may result in NIR-responsive hyperthermia generation for PTT as well as further induce the liquid–gas phase transformation of PFP. A series of therapeutic evaluations both in vitro and in vivo confirmed the superior synergistic chemo-PTT efficacy of our PHDP. The unique tumor-specific biodegradation and low observable toxicity facilitated its applications in therapeutic applications. It is thus expected that PHDP nanoparticles may be served as a promising nanotheranostic agent for US imaging and efficient chemo-PTT synergistic treatment of other tumor types.

Acknowledgment

This study was supported by the National Natural Science Foundation of China (No. 81571677, 81571679 and 81771838).

Disclosure

The authors report no conflicts of interest in this work.

References

1. Bray F, Ferlay J, Soerjomataram I, et al. Global cancer statistics 2018: GLOBOCAN estimates of incidence and mortality worldwide for 36 cancers in 185 countries. *CA Cancer J Clin*. 2018;68(6):394–424. doi:10.3322/caac.21492
2. Torre LA, Trabert B, DeSantis CE, et al. Ovarian cancer statistics, 2018. *CA Cancer J Clin*. 2018;68(4):284–296. doi:10.3322/caac.21456
3. Yang PP, Luo Q, Qi GB, et al. Host materials transformable in tumor microenvironment for homing theranostics. *Adv Mater*. 2017;17(15):1605869. doi:10.1002/adma.201605869
4. Fan W, Yung B, Huang P, Chen X. Nanotechnology for multimodal synergistic cancer therapy. *Chem Rev*. 2017;117(22):13566–13638. doi:10.1021/acs.chemrev.7b00258
5. McGranahan N, Swanton C. Clonal heterogeneity and tumor evolution: past, present, and the future. *Cell*. 2017;168(4):613–628. doi:10.1016/j.cell.2017.01.018
6. Lim EK, Kim T, Paik S, et al. Nanomaterials for theranostics: recent advances and future challenges. *Chem Rev*. 2015;115(1):327–394. doi:10.1021/cr300213b
7. Kiessling F, Fokong S, Bzyl J, et al. Recent advances in molecular, multimodal and theranostic ultrasound imaging. *Adv Drug Deliv Rev*. 2014;72:15–27. doi:10.1016/j.addr.2013.11.013
8. Yang B, Chen Y, Shi J. Material chemistry of two-dimensional inorganic nanosheets in cancer theranostics. *Chem*. 2018;4(6):1284–1313.
9. Ehlerding EB, Chen F, Cai W. Biodegradable and renal clearable inorganic nanoparticles. *Adv Sci*. 2016;3(2):1500223. doi:10.1002/advs.201500223

10. Naz S, Shamoon M, Wang R, Zhang L, Zhou J, Chen J. Advances in therapeutic implications of inorganic drug delivery nano-platforms for cancer. *Int J Mol Sci*. 2019;20(4):965. doi:10.3390/ijms20040965
11. Zhang L, Qiao S, Jin Y, et al. Magnetic hollow spheres of periodic mesoporous organosilica and Fe_3O_4 nanocrystals: fabrication and structure control. *Adv Mater*. 2008;20(4):805–809. doi:10.1002/adma.200700900
12. Zheng Y, Wang D, Li Z, et al. Laccase biosensor fabricated on flower–shaped yolk–shell SiO_2 nanospheres for catechol detection. *Colloid Surface A*. 2018;538:202–209. doi:10.1016/j.colsurfa.2017.10.086
13. Huang P, Chen Y, Lin H, et al. Molecularly organic/inorganic hybrid hollow mesoporous organosilica nanocapsules with tumor-specific biodegradability and enhanced chemotherapeutic functionality. *Biomaterials*. 2017;125:23–37. doi:10.1016/j.biomaterials.2017.02.018
14. Wu J, Bremner DH, Niu S, et al. Functionalized MoS_2 nanosheet-capped periodic mesoporous organosilicas as a multifunctional platform for synergistic targeted chemo-photothermal therapy. *Chem Eng J*. 2018;342:90–102. doi:10.1016/j.cej.2018.02.052
15. Chen Y, Meng Q, Wu M, et al. Hollow mesoporous organosilica nanoparticles: a generic intelligent framework-hybridization approach for biomedicine. *J Am Chem Soc*. 2014;136(46):16326–16334. doi:10.1021/ja508721y
16. Yu L, Chen Y, Lin H, Du W, Chen H, Shi J. Ultrasmall mesoporous organosilica nanoparticles: morphology modulations and redox-responsive biodegradability for tumor-specific drug delivery. *Biomaterials*. 2018;161:292–305. doi:10.1016/j.biomaterials.2018.01.046
17. Wong PT, Choi SK. Mechanisms of drug release in nanotherapeutic delivery systems. *Chem Rev*. 2015;115(9):3388–3432. doi:10.1021/cr5004634
18. Lu N, Huang P, Fan W, et al. Tri-stimuli-responsive biodegradable theranostics for mild hyperthermia enhanced chemotherapy. *Biomaterials*. 2017;126:39–48. doi:10.1016/j.biomaterials.2017.02.025
19. Li Z, Han J, Yu L, et al. Synergistic sonodynamic/chemotherapeutic suppression of hepatocellular carcinoma by targeted biodegradable mesoporous nanosonosensitizers. *Adv Funct Mater*. 2018;28(26):1800145. doi:10.1002/adfm.201800145
20. Wu J, Bremner DH, Niu S, et al. Chemodrug-gated biodegradable hollow mesoporous organosilica nanotheranostics for multimodal imaging-guided low-temperature photothermal therapy/chemotherapy of cancer. *ACS Appl Mater Interfaces*. 2018;10(49):42115–42126. doi:10.1021/acsami.8b16448
21. Zheng Y, Wang L, Krupka TM, et al. The feasibility of using high frequency ultrasound to assess nerve ending neuropathy in patients with diabetic foot. *Eur J Radiol*. 2013;82(3):512–517. doi:10.1016/j.ejrad.2012.09.017
22. Wang H, Hristov D, Qin J, Tian L, Willmann JK. Three-dimensional dynamic contrast-enhanced US imaging for early antiangiogenic treatment assessment in a mouse colon cancer model. *Radiology*. 2015;277(2):424–434. doi:10.1148/radiol.2015142824
23. Lee J, Min HS, You DG, et al. Theranostic gas-generating nanoparticles for targeted ultrasound imaging and treatment of neuroblastoma. *J Control Release*. 2016;223:197–206. doi:10.1016/j.jconrel.2015.12.051
24. Tang H, Zheng Y, Chen Y. Materials chemistry of nanoultrasonic biomedicine. *Adv Mater*. 2017;29(10):1604105. doi:10.1002/adma.201700681
25. Kyung HM, Hong JL, Dong JP, et al. pH-controlled gas-generating mineralized nanoparticles: a theranostic agent for ultrasound imaging and therapy of cancers. *ACS Nano*. 2015;9(1):134–145. doi:10.1021/nn506210a
26. Kim M, Lee JH, Kim SE, Kang SS, Tae G. Nanosized ultrasound enhanced-contrast agent for in vivo tumor imaging via intravenous injection. *ACS Appl Mater Interfaces*. 2016;8(13):8409–8418. doi:10.1021/acsami.6b02115
27. Zhao Y, Song W, Wang D, et al. Phase-shifted PFH@PLGA/Fe_3O_4 nanocapsules for MRI/US imaging and photothermal therapy with near-infrared irradiation. *ACS Appl Mater Interfaces*. 2015;7(26):14231–14242. doi:10.1021/acsami.5b01873
28. Lu N, Fan W, Yi X, et al. Biodegradable hollow mesoporous organosilica nanotheranostics for mild hyperthermia-induced bubble-enhanced oxygen-sensitized radiotherapy. *ACS Nano*. 2018;12(2):1580–1591. doi:10.1021/acsnano.7b08103
29. Fokong S, Theek B, Wu Z, et al. Image-guided, targeted and triggered drug delivery to tumors using polymer-based microbubbles. *J Control Release*. 2012;163(1):75–81. doi:10.1016/j.jconrel.2012.07.028
30. Jia X, Cai X, Chen Y, et al. Perfluoropentane-encapsulated hollow mesoporous prussian blue nanocubes for activated ultrasound imaging and photothermal therapy of cancer. *ACS Appl Mater Interfaces*. 2015;7(8):4579–4588. doi:10.1021/am507443p
31. Wu S, Mou C, Lin H. Synthesis of mesoporous silica nanoparticles. *Chem Soc Rev*. 2013;42(9):3862–3875. doi:10.1039/c3cs35405a
32. Parambadath S, Mathew A, Jenisha B, et al. A pH-responsive drug delivery system based on ethylenediamine bridged periodic mesoporous organosilica. *Micropor Mesopor Mat*. 2015;215:67–75. doi:10.1016/j.micromeso.2015.05.027
33. Wang X, Chen H, Chen Y, et al. Perfluorohexane-encapsulated mesoporous silica nanocapsules as enhancement agents for highly efficient high intensity focused ultrasound (HIFU). *Adv Mater*. 2012;24(6):785–791. doi:10.1002/adma.201104033
34. Min HS, You DG, Son S, et al. Echogenic glycol chitosan nanoparticles for ultrasound-triggered cancer theranostics. *Theranostics*. 2015;5(12):1402–1418. doi:10.7150/thno.13099
35. Ji X, Kong N, Wang J, et al. A novel top-down synthesis of ultrathin 2D boron nanosheets for multimodal imaging-guided cancer therapy. *Adv Mater*. 2018;30(36):1803031. doi:10.1002/adma.201803031